IEEE Access
Multidisciplinary | Rapid Review | Open Access Journal

Received 1 May 2023, accepted 13 June 2023, date of publication 21 June 2023, date of current version 28 June 2023.

Digital Object Identifier 10.1109/ACCESS.2023.3288282

RESEARCH ARTICLE

Small-Signal Stability Analysis of Three-Phase Four-Wire System Integrated With Single-Phase PV Inverters Considering Phase to Phase Coupling Effect Under Asymmetric Grid

YUMING LIAO, HENG NIAN, (Senior Member, IEEE), YAOXIN WANG, (Student Member, IEEE), AND DAN SUN, (Senior Member, IEEE)
College of Electrical Engineering, Zhejiang University, Hangzhou 310027, China
Corresponding author: Heng Nian (nianheng@zju.edu.cn)

This work was supported by the National Natural Science Foundation of China under Grant 51977194.

ABSTRACT With the rapid growth of renewable energy sources, single-phase rooftop photovoltaic inverters connected to the distribution network have received widespread applications in recent years. In such a distribution network, asymmetric fault problems are likely to occur, and small-signal stability during asymmetric faults becomes important. The existing papers analyzed the sequence impedance and related stability issues during asymmetric faults in a three-phase three-wire system. In contrast, the SIs connected to three-phase four-wire systems requires consideration of the effect of zero-sequence components and the phase to phase coupling effect. Because both the zero-sequence component and phase coupling effect will affect the impedance characteristics of the inverter sub-system and thus the stability of the power system. Therefore, this paper established the 3∗3 admittance model matrix for the inverter sub-system considering the frequency coupling effect and phase coupling effect under asymmetric fault. Based on the admittance model matrix, the main factors including phase-locked loop bandwidth and grid neutral inductance that affects the phase to phase coupling effect are also analyzed. In addition, this paper studies the effect of phase-locked loop bandwidth, short circuit fault degree, and short circuit location on system stability. The validity of theoretical analysis is further verified through the experimental results.

INDEX TERMS Asymmetric fault, impedance-based stability theory, phase to phase coupling effect, single-phase rooftop photovoltaic inverter, three-phase four-wire system.

I. INTRODUCTION

Distribution power systems are undergoing significant evolutions in physical and technical features due to the large-scale integration of rooftop solar photovoltaics driven by falling prices and technological improvements [1], [2]. The configuration shown in Figure 1 becomes a common scenario [3], [4], [5], [6], [7], [8] in which single-phase rooftop photovoltaic inverters (SIs) are divided into three phase groups and connected to the three-phase four-wire distribution grid in star(Y) configuration.

The associate editor coordinating the review of this manuscript and approving it for publication was Xueguang Zhang.

The interactions between the weak grid and converters may cause system instability [9], [10], [11]. And the impedance-based stability analysis method is proved applicable and useful to analyze the small signal stability of the grid-connected system since the impedances of the grid and inverters can be easily obtained from either the analytical impedance model [9], [10], [11], [12] or the measured impedance with clear physical meanings [13], [14], [15].

Many efforts have been taken to develop impedance models and small-signal stability analysis of single-phase inverters in [12], [13], [14], [15], [16], [17], [18], [19], and [20]. Reference [12] established an impedance model of the single-phase PV inverter and proposed a method to

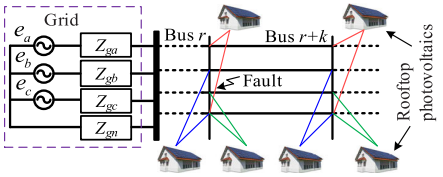

FIGURE 1. Structure of SIs connected to the three-phase four-wire grid.

improve the system stability by introducing phase lead compensation to the control structure. References [17], [18], [19], and [20] analyzed the frequency- coupling effect in the single-phase grid-connected inverter system, which indicates that the frequency coupling effect (FCE) makes a significant difference in system stability. Reference [18] established a 3∗3 impedance model to capture the coupling frequency components with improved accuracy. References [19] and [20] developed the single input single output (SISO) impedance model of the single-phase inverter considering FCE, which makes it intuitive to identify the stability of the system. However, the relevant papers on the stability analysis of single-phase inverters paid main attention to the stability when the single-phase inverters are connected to single-phase grids under normal operating situations without considering the stability issue during the fault state.

Based on existing research, it has been found that small-signal instability is more likely to occur in voltage source converter (VSC) systems connected to weak grids during fault steady state [21], [22], [23], [24], [25], [26], [27], [28], [29], [30], [31]. Recent papers have examined the small-signal stability of these systems during fault steady state. For example, [22] establishes a dynamic model of the VSC during low voltage ride through (LVRT) to analyze the effect of the phase-locked loop (PLL) on system stability and proposes a control strategy to address stability issues. References [23] and [24] analyze the stability of renewable energy inverter systems connected to weak grids during LVRT and indicate that stability is mainly influenced by the interaction between the PLL and current control loops.

The stability analysis of VSC-based converter systems during asymmetric grid faults is more complicated due to the presence of the negative sequence components compared to the symmetric grid faults [25]. In [25], the analytical model of the VSC grid-connected system during an asymmetric network has been established in synchronous rotation frames of the sequence domain to explore the VSC dynamic characteristics. In [26], the effects of various control coefficients on the stability during asymmetric faults have been investigated. References [27], [28], [29], [30], and [31] established analytical models and investigates the effect of frequency-coupling effect on system stability during asymmetric grid. According to the literatures [21], [22], [23], [24], [25], [26], [27], [28], [29], [30], [31], it can be found that the investigations on impedance modeling and stability analysis for three-phase three-wire grid-connected system during grid fault state have achieved plentiful investigations.

However, it should be noted that these findings are more applicable to three-phase three-wire converters. In contrast, the stability analysis of the scene that SIs connected to the three-phase four-wire grid, shown in Figure 1, needs to consider not only the effects of positive and negative sequence components but also the influence of zero sequence components. Because there is not only the coupling relationship between the positive sequence (PS) component and the negative sequence (NS) component, but also the coupling relationship between the zero sequence (ZS) component and the PS component as well as the NS component. In addition, asymmetric short-circuit faults can also lead to changes in grid-side impedance, further leading to the stronger coupling between PS, NS and ZS impedances of the grid. This coupling relationship further increases the coupling degree of the entire system, thus also increasing the difficulty of system stability analysis.

In addition, there is also a phase to phase coupling effect (PPCE) between the three phases inverters since the output currents and voltages of the phase-*a*, phase-*b*, and phase-*c* converters will interact with each other through the neutral line inductance [5], [6], [7], [8]. The interaction between three phases results in significant differences in the small signal disturbance loop of the SIs connected to the three-phase four-wire grid system compared to the small signal disturbance loop of the SI connected to the single-phase grid system as shown in [12], [13], [14], [15], [16], [17], [18], [19], and [20]. And the difference in the small signal disturbance loop will lead to errors when the models without considering the PPCE are used to implement the stability analysis. Additionally, the frequency coupling effect is also observed in single-phase inverters. When the phase to phase coupling effect and the frequency coupling effect are present in the system at the same time, a small-signal model that can characterize and analyze both effects is necessary and important. However, the traditional small-signal loop analysis method based on positive, negative, and zero sequence components is too complicated to build such a small-signal model due to the complex FCE inside the inverters and the complicated coupling relationship between the inverters and asymmetrical grid.

In summary, the stability issue of single-phase inverters connected to single-phase grids and the instability of three-phase three-wire converters under fault grids have received extensive attention and research. However, the stability analysis of a three-phase four-wire system integrated with single-phase inverters considering phase to phase coupling effect under an asymmetric grid has not received much attention and sufficient investigation. And relevant literatures are lacking. In order to fill this gap, the paper integrates the effect of the PPCE and FCE into impedance modeling through harmonics linearization and analyzes the influence of dominant parameters on the system stability.

The contributions and main works of the paper could be summarized as (1) The paper analyzes the PPCE due to the interaction between different phase inverters, and reveals the effect law of PLL parameters and neutral line inductance on the PPCE; (2) The small-signal model and impedance model of the inverter system considering the FCE, PPCE and asymmetric grid is established, which provides an accurate description to the small-signal perturbation components during asymmetric short-circuit faults; (3) Based on the achieved impedance model, small-signal stability analysis of the system during asymmetric grid fault has been analyzed, which reveals that the influence laws of the bandwidth of PLL, the degree of short circuit fault and the location of short circuit on the system stability.

And this paper is organized as follows: Section II shows the configuration of the investigated SIs connected to the three-phase four-wire weak grid during asymmetrical grid and the mechanism of PPCE generation in the system. Section III establishes and verifies the detailed impedance model of the inverter sub-system considering FCE and PPCE under asymmetric fault. Besides, the dominant parameters which have an effect on the PPCE are also analyzed in Section III. Section IV implements the system stability analysis as well as investigates the effect of PLL bandwidth, short circuit fault degree, and short circuit location on system stability. To verify the developed impedance models and the accuracy of analysis results, the experimental results are shown in Section V. Finally, Section VI shows the conclusion of this paper.

II. CONFIGURATION AND CONTROL METHOD OF THE INVESTIGATED SYSTEM

As mentioned in the introduction, the paper focuses on the small-signal system stability of SIs connected to three-phase four-wire week grid. The general configuration and control strategy of SIs can be depicted in Figure 2. The SIs are grouped into three phases, which are commonly connected with star(Y) configuration as shown in Figure 2(a). SI*a*, SI*b*, and SI*c* are the three SIs shown in Figure 2(b). The inverter shown in Figure 2(b) is considered decoupled with the photovoltaic source due to the large capacitors [29]. it is also practically reasonable when the bandwidth of the DC voltage loop is relatively lower than the PLL bandwidth [30].

The classical current control strategy of the inverter depicted in Figure 2(c) is applied in this paper. In Figure 2(c), *Gf* is the PCC voltage feedforward gain, which is selected as 0.6 [33], [34] to improve the robustness of the system. kc is the capacitor current feedforward gain. G_d is the control delay, where $G_d = e^{-1.5T_s}$. T_s is the control period. And Gc is the proportional-resonant (PR) regulator.

In order to better present the PPCE, the output port of SIa is injected with a harmonic voltage at 130 Hz. Figure 3 shows the experimental waveforms of inverters SI*a*, SI*b* and SI*c*. Figure 3(a) and Figure 3(b) show the voltages, currents

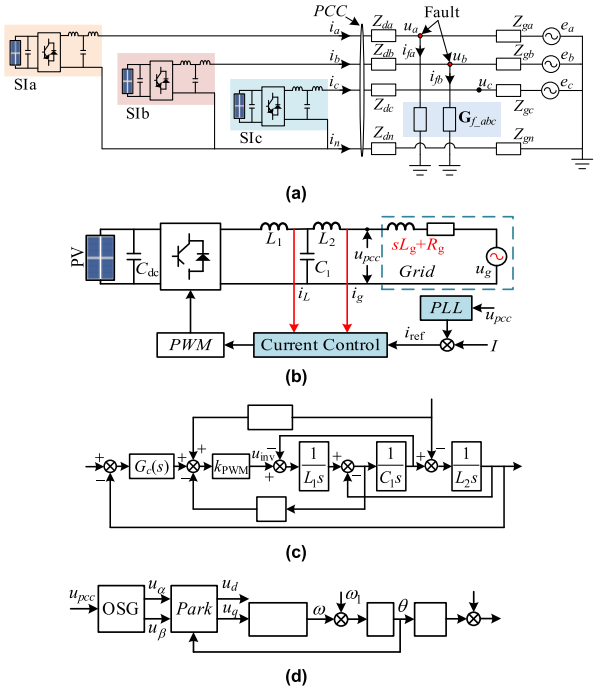

FIGURE 2. Schematic and control strategy of the investigated system. (a) Configurations of SIs connected to three-phase four-wire weak grid. (b) Schematic of the SI connected to the weak grid. (c) The control block of the current controller. (d) The control block of the PLL.

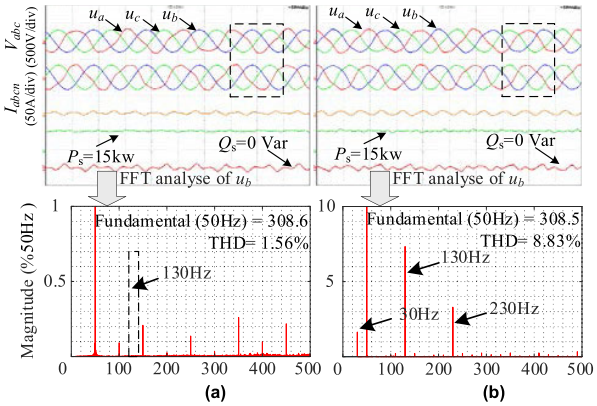

FIGURE 3. Experimental waveforms when the output port of SIa is injected with a harmonic voltage at 130Hz. (a) when the neutral inductances of the grid Lgnt = 0 mH. (b) when the neutral inductances of the grid Lgnt = 4 mH.

and powers when the total neutral inductances of the grid ($L_{gnt} = L_{dn} + L_{gn}$) equals 0mH and 4mH respectively. And the other parameters can be seen in Table 1. From Figure 3(a), it can be seen that there is no harmonic voltage at 130Hz in SI*b* and SI*c* since PCCE does not exist in three phases and the harmonic components produced by SIs cannot transmit to SI*b* and SI*c*. On the contrary, it can be seen from Figure 3 (b) that the harmonic voltage at 130 Hz also appears in SI*b*, of course, SI*c*, due to the PPCE transmitted from SI*a*. And the harmonic voltages at 30Hz and 230Hz are caused by the FCE.

PPCE makes output voltages and currents of each phase inverter affect each other, which makes the stability analysis of the system need to consider the coupling effect between

the three phases. The next section will deduce the impedance of the SIs and the inverter sub-system.

III. IMPEDANCE MODELING OF THE THREE-PHASE FOUR-WIRE SYSTEM DURING ASYMMETRIC FAULTS OF WEAK GRID

This section first briefly introduces the impedance model of the SI considering the initial phase of phase-a phase-b and phase-c grid voltages and then builds the impedance model of the inverter sub-system.

A. IMPEDANCE MODEL OF THE INVERTER SUB-SYSTEM CONSIDERING FCE AND PPCE

The impedance model of SI is presented as shown in equation (1). Figure 4 shows the voltage and current small-signal path figures of the SI, from which it can be seen that in addition to the current and voltage components with a perturbation frequency ω there are also voltage and current components with frequency $\omega \pm 2j\omega_1$ in the system due to the FCE. The $\omega_1 = 2\pi f_1$, f_1 is the rated frequency of the grid. In Figure 4, s represents the Laplace operator. s^- represents negatively coupled frequency $s - 2j\omega_1$. And s^+ represents the positively coupled frequency $s + 2j\omega_1$.

From Figure 4 it can be seen that the grid current i_g at frequencies $\omega - 2j\omega_1$, ω, and $\omega + 2j\omega_1$ can be obtained as

$$\begin{bmatrix} i_{gx}(s^-) \\ i_{gx}(s) \\ i_{gx}(s^+) \end{bmatrix} = \left(\mathbf{Y_{xref}}(s) + \mathbf{Y_{xinvo}}(s)\right) \begin{bmatrix} u_{xpcc}(s^-) \\ u_{xpcc}(s) \\ u_{xpcc}(s^+) \end{bmatrix} \quad (1)$$

where, $\mathbf{Y_{xinvo}}(s) = [Y_{xio}(s^-), 0, 0; 0\ Y_{xio}(s), 0; 0, 0\ Y_{xio}(s^+)]$ and $\mathbf{Y_{xref}}(s)$ can be obtained as equation (2).

$$\mathbf{Y_{xref}}(s) = \begin{bmatrix} Y_{xref0}(s^-) & Y_{xref+}(s^-) & 0 \\ Y_{xref-}(s) & Y_{xref0}(s) & Y_{xref+}(s) \\ 0 & Y_{xref-}(s^+) & Y_{xref0}(s^+) \end{bmatrix} \quad (2)$$

$Y_{xref-}(s)$, $Y_{xref0}(s)$, and $Y_{xref+}(s)$ represent the transfer relationship from voltage u_{pcc} at frequency $\omega + 2j\omega_1$, ω, and ω-$2j\omega_1$ to current i_g at frequency ω respectively. And the responding mathematical expressions can be expressed as

$$Y_{xref0}(s) = I_{xref0}(s)\, G_{plant}(s) \quad (3)$$

$$Y_{xref+}(s^+) = I_{xref+}(s^+)\, G_{plant}(s^+) \quad (4)$$

$$Y_{xref-}(s^-) = I_{xref-}(s^-)\, G_{plant}(s^-) \quad (5)$$

$$\begin{aligned} I_{xref0}(s) = {} & 0.25 I_{ref}\left[\tilde{u}_\alpha(s) + j\tilde{u}_\beta(s)\right] G_{xpll}(s - j\omega_1) \\ & + 0.25 I_{ref}\left[\tilde{u}_\alpha(s) - j\tilde{u}_\beta(s)\right] G_{xpll}(s + j\omega) \end{aligned} \quad (6)$$

$$\begin{aligned} I_{xref+}(s) = {} & -0.25 e^{-j2\phi_{vx}} I_{ref}\tilde{u}_\alpha(s + 2j\omega_1)\, G_{xpll}(s + j\omega_1) \\ & - 0.25 j e^{-j2\phi_{vx}} I_{ref}\tilde{u}_\beta(s + 2j\omega_1)\, G_{xpll}(s + j\omega_1) \end{aligned} \quad (7)$$

$$\begin{aligned} I_{xref-}(s) = {} & -0.25 e^{j2\phi_{vx}} I_{ref}\tilde{u}_\alpha(s - 2j\omega_1)\, G_{xpll}(s - j\omega_1) \\ & + j0.25 e^{j2\phi_{vx}} I_{ref}\tilde{u}_\beta(s - 2j\omega_1)\, G_{xpll}(s - j\omega_1) \end{aligned} \quad (8)$$

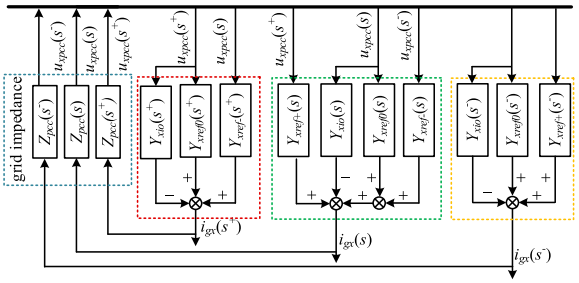

FIGURE 4. Voltage and current small signal path diagram of SI.

$$G_{xplant} = \frac{G_c G_d}{s^3 L_1 L_2 C + G_c G_d s^2 L_2 C + G_d G_c + sL_1 + sL_2} \quad (9)$$

$$Y_{xio}(s) = \frac{1 + s^2 L_1 C + sCk_c G_d - G_f G_d}{s^3 L_1 L_2 C + k_c G_d s^2 L_2 C + G_d G_c + sL_1 + sL_2} \quad (10)$$

$$G_{xpll}(s) = \frac{G_{xPI}(s)}{s + U_m G_{xPI}(s)} = \frac{k_{xpp} + k_{xii}/s}{s + U_m\left(k_{xpp} + k_{xii}/s\right)} \quad (11)$$

The subscript "x" in (1) to (11) denotes the variables in phase-a, phase-b, or phase-c. ϕ_{vx} denotes the initial phase of the grid. The $G_{OSG\alpha}$ and $G_{OSG\beta}$ denote the transfer function from u_{PCC} to u_α and u_β respectively. Without loss of the generality, the time delay-based PLL [12], [17] is also applied in the paper, which can be expressed as (12). $T_0 = 0.02$ s, which is the period of the grid voltage.

$$\begin{cases} u_\alpha(s) = G_{osg\alpha}(s)\, u_{pcc}(s) = u_{pcc}(s) \\ u_\beta(s) = G_{osg\beta}(s)\, u_{pcc}(s) = u_{pcc}(s)\, e^{-T_0 s/4} \end{cases} \quad (12)$$

Figure 5 shows the three-phase four-wire system small-signal models considering the PPCE and FCE during asymmetric fault. Figure 5(a) shows the variables with the perturbation frequency ω. In Figure 5(a), the admittance elements Y_{SIoa}, Y_{SIob} and Y_{SIoc} denote the input admittance of SIa, SIb, and SIc at ω respectively. And the Y_{SIox} can be defined by $Y_{xref0}(s) + Y_{xio}(s)$. Similarly, the variables in Figure 5(b) and Figure 5(c) are at the coupling frequency $\omega + 2j\omega_1$ and $\omega - 2j\omega_1$ respectively. Z_{dx} and Z_{gx} represent the grid impedance of phase-x. G_{fa} and G_{fb} denote the fault admittance of the fault branch in phase-a and phase-b.

The coupling relationship between three circuits is modeled by the controlled current sources in Figure 5. The controlled current sources i^1_{a+2} is determined by the voltage difference $u^{+2}_a - u^{+2}_n$, which represents the current component at frequency ω produced by the voltage across SIa at frequency $\omega + 2j\omega_1$. Correspondingly, the controlled current sources i^1_{a-2} is determined by voltage difference $u^{-2}_a - u^{-2}_n$, which represents the current component at frequency ω produced by the voltage across SIa at frequency $\omega - 2j\omega_1$. And the definitions of the controlled current sources in SIb and SIc are similar to SIa.

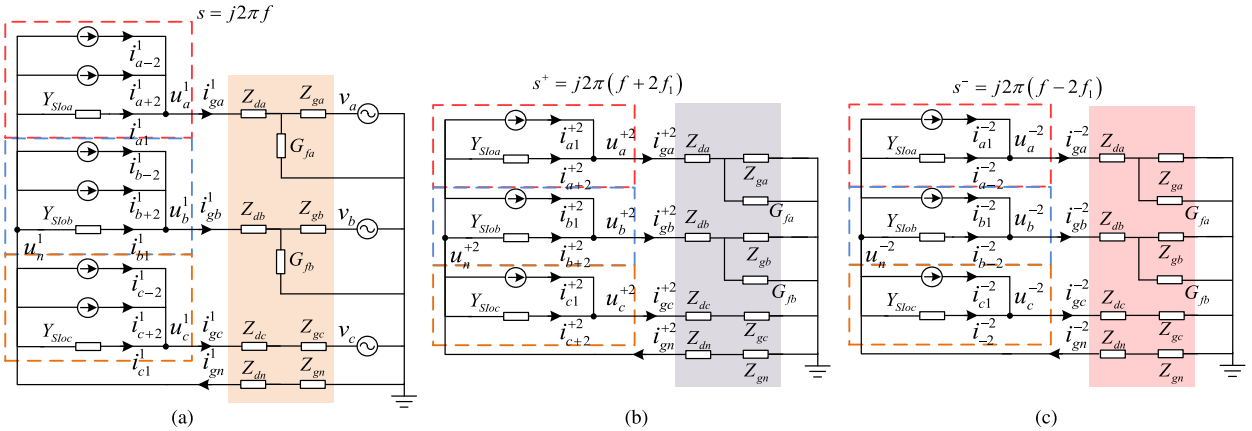

FIGURE 5. Three-phase four-wire system small-signal models considering frequency coupling effect and phase coupling effect. (a) system small-signal models at frequency ω. (b) system small-signal models at frequency $\omega + 2j\omega_1$. (c) system small-signal models at frequency $\omega - 2j\omega_1$.

According to Figure 5(a), the following expression can be achieved as,

$$\begin{bmatrix} u_a^1 - u_n^1 \\ u_b^1 - u_n^1 \\ u_c^1 - u_n^1 \end{bmatrix} = \begin{bmatrix} u_{an}^1 \\ u_{bn}^1 \\ u_{cn}^1 \end{bmatrix} = \mathbf{Z_{s3}}(s) \begin{bmatrix} i_{ga}^1 \\ i_{gb}^1 \\ i_{gc}^1 \end{bmatrix} + \begin{bmatrix} v_a^1 \\ v_b^1 \\ v_c^1 \end{bmatrix} \quad (13)$$

And (14) shows the grid impedance matrix.

$$\mathbf{Z_{s3}}(s) = \mathbf{Z_D}(s) + \mathbf{Z_{DN}}(s) + \mathbf{Z_G}(s)(\mathbf{I} + \mathbf{Z_G}(s)\mathbf{G_f}(s))^{-1} \quad (14)$$

where, $\mathbf{Z_D}(s) = \text{diag}(Z_{da}(s), Z_{db}(s), Z_{dc}(s))$, $\mathbf{Z_{DN}}(s) = (Z_{dn}(s) + Z_{gn}(s))\mathbf{E}$. And $\mathbf{E}$ is the identity matrix. Impedance matrix $\mathbf{Z_G}(s) = \text{diag}(Z_{ga}(s), Z_{gb}(s), Z_{gc}(s))$, and the admittance matrix of the fault branches can be obtained as $\mathbf{G_f}(s) = \text{diag}(G_{fa}(s), G_{fb}(s), G_{fc}(s))$. Defining $Z_dys) = sL_{dy} + R_{dy}$ and $Z_{gy}(s) = sL_{gy} + R_{gy}$, $y = a, b, c, n$, denote the grid impedances. $G_{fx}(s) = 1/sL_{fx} + 1/R_{fx}$, $x = a, b, c$, denote the fault admittance of the phase-x.

From Figure 5(a), the grid current can be expressed as,

$$\begin{bmatrix} i_{ga}^1 \\ i_{gb}^1 \\ i_{gc}^1 \end{bmatrix} = \begin{bmatrix} i_{a-2}^1 \\ i_{b-2}^1 \\ i_{c-2}^1 \end{bmatrix} + \begin{bmatrix} i_{a+2}^1 \\ i_{b+2}^1 \\ i_{c+2}^1 \end{bmatrix} + \begin{bmatrix} i_{a1}^1 \\ i_{b1}^1 \\ i_{c1}^1 \end{bmatrix} \quad (15)$$

In Figure 5(a), the controlled current sources i_{a-2}^1, i_{b-2}^1, and i_{c-2}^1 denote the current component at frequency ω excited by voltage across SIa, SIb, and SIc respectively at frequency $\omega - 2j\omega_1$.

Thus, according to (1) and (2), the i_{a-2}^1, i_{b-2}^1, and i_{c-2}^1 can be obtained as,

$$\mathbf{I_{-2}^1}(s) = \mathbf{Y^{C+2}}(s)\mathbf{U^{-2}}(s^-) \quad (16)$$

where, $\mathbf{Y^{C+2}}(s) = \text{diag}(Y_{aref-}(s), Y_{bref-}(s), Y_{cref-}(s))$, which is the 3∗3 diagonal matrix. $Y_{aref-}(s)$, $Y_{bref-}(s)$, $Y_{cref-}(s)$ can be obtained from (5). Denote $\mathbf{I_{-2}^1}(s) = [i_{a-2}^1(s), i_{b-2}^1(s), i_{c-2}^1(s)]^{\mathrm{T}}$, $\mathbf{U^{-2}}(s) = [u_{an}^{-2}(s^-), u_{bn}^{-2}(s^-), u^-2_{cn}(s^-)]^{\mathrm{T}}$.

Similarly, the controlled current sources i_{a+2}^1, i_{b+2}^1 and i_{c+2}^1 can be obtained as,

$$\mathbf{I_{+2}^1}(s) = \mathbf{Y^{C-2}}(s)\mathbf{U^{+2}}(s^+) \quad (17)$$

where, $\mathbf{Y^{C-2}}(s) = \text{diag}(Y_{aref+}(s), Y_{bref+}(s), Y_{cref+}(s))$, which is the 3∗3 diagonal matrix. $Y_{aref+}(s)$, $Y_{bref+}(s)$, $Y_{cref+}(s)$ can be obtained from (4). Denote $\mathbf{I_{+2}^1}(s) = [i_{a+2}^1(s), i_{b+2}^1(s), i_{c+2}^1(s)]^{\mathrm{T}}$, $\mathbf{U^{+2}}(s^+) = [u_{an}^{+2}(s^+), u_{bn}^{+2}(s^+), u_{cn}^{+2}(s^+)]^{\mathrm{T}}$.

The currents i_{a1}^1, i_{b1}^1 and i_{c1}^1 denote the current component at frequency ω excited by the voltage across the single inverters at frequency ω, which can be expressed as (18).

$$\mathbf{I_1^1}(s) = \mathbf{Y_{SIO}}(s)\mathbf{U^1}(s) \quad (18)$$

where, $\mathbf{Y_{SIO}}(s) = \text{diag}(Y_{SIOa}(s), Y_{SIOb}(s), Y_{SIOc}(s))$, which is a 3∗3 diagonal matrix. $Y_{SIOx}(s) = I_{xref0}(s) + Y_{io}(s)$, x = a, b, c denotes phase-x. Denote $\mathbf{I_1^1}(s)[i_{a1}^1, i_{b1}^1, i_{c1}^1]^{\mathrm{T}}$, $\mathbf{U^1}(s) = [u_{an}^1(s), u_{bn}^1(s), u_{cn}^1(s)]$.

From Figure 5(b), the controlled current sources i_{a1}^{+2}, i_{b1}^{+2} and i_{c1}^{+2} represent current with frequency $\omega + 2j\omega_1$ produced by voltage across SIa, SIb and SIc respectively at frequency ω, which can be expressed as,

$$\mathbf{I_1^{+2}}(s^+) = \mathbf{Y^{C+2}}(s^+)\mathbf{U^1}(s^+) \quad (19)$$

where, $\mathbf{Y^{C+2}}(s^+) = \text{diag}(Y_{aref-}(s^+), Y_{bref-}(s^+), Y_{cref-}(s^+))$, which is a diagonal matrix. Denote $\mathbf{I_1^{+2}}(s^+) = [i_{a1}^{+2}(s^+), i_{b1}^{+2}(s^+), i_{c1}^{+2}(s^+)]^{\mathrm{T}}$, $\mathbf{U^1}(s)[u_{an}^1(s), \mathbf{U^1}(s)u_{bn}^1(s), \mathbf{U^1}(s)u_{cn}^1(s)]^{\mathrm{T}}$.

Similarly, the current i_{a+2}^{+2}, i_{b+2}^{+2} and i_{c+2}^{+2} denotes the current component with frequency $\omega + 2j\omega_1$ excited by voltage across SIa, SIb and SIc respectively at frequency $\omega + 2j\omega_1$, which can be expressed as,

$$\mathbf{I_{+2}^{+2}}(s^+) = \mathbf{Y_{SIO}}(s^+)\mathbf{U^{+2}}(s^+) \quad (20)$$

where, $\mathbf{Y_{SIO}}(s^+) = \text{diag}(Y_{SIOa}(s^+), Y_{SIOb}(s^+), Y_{SIOc}(s^+))$, it's a 3∗3 diagonal matrix. Denote $Y_{SIOx}(s^+) = I_{xref0}(s^+) + Y_{io}(s^+)$. The current matrix $\mathbf{I_{+2}^{+2}}(s^+)$ and voltage matrix $\mathbf{U^{+2}}(s^+)$ can be expressed as $\mathbf{I_{+2}^{+2}} =$

$[i^{+2}_{a+2}(s^+), i^{+2}_{b+2}(s^+), i^{+2}_{c+2}(s^+)]^{\mathrm{T}}$ and $\mathbf{U^{+2}}(s^+) = [u^1_{an}(s^+), u^1_{bn}(s^+), u^1_{cn}(s^+)]^{\mathrm{T}}$.

From Figure 5(b), the grid currents and the terminal voltages of the inverter sub-system at frequency $\omega + 2j\omega_1$ can be obtained as,

$$\mathbf{U^{+2}}\left(s^+\right) = \mathbf{Z_{s3}}\left(s^+\right)\left(\mathbf{I_1^{+2}}\left(s^+\right) + \mathbf{I_{+2}^{+2}}\left(s^+\right)\right). \quad (21)$$

Combing (16), (17) and (28), the relationship between terminal voltages of the inverter sub-system at frequency $\omega + 2j\omega_1$ and ω can be achieved as (19). Matrix $\mathbf{I}$ is the diagonal unit matrix.

$$\mathbf{U^{+2}}\left(s^+\right) = \left[\mathbf{I} - \mathbf{Z_{s3}}\left(s^+\right)\mathbf{Y_{SIO}}\left(s^+\right)\right]^{-1}\mathbf{Z_{s3}}\left(s^+\right) \times \mathbf{Y^{C+2}}\left(s^+\right)\mathbf{U}^1\left(s\right) \quad (22)$$

Similarly, the relationship between terminal voltages of the inverter sub-system at frequency $\omega - 2j\omega_1$ and ω can be achieved as,

$$\mathbf{U^{-2}}\left(s^-\right) = \left[\mathbf{I} - \mathbf{Z_{s3}}\left(s^-\right)\mathbf{Y_{SIO}}\left(s^-\right)\right]^{-1}\mathbf{Z_{s3}}\left(s^-\right) \times \mathbf{Y^{C-2}}\left(s^-\right)\mathbf{U}^1\left(s\right) \quad (23)$$

Combining (15), (22), and (23), the impedance model of the inverter sub-system can be expressed as (24).

$$\begin{aligned}\mathbf{I}^1\left(s\right) &= \mathbf{Y_{SIO}}\left(s\right)\mathbf{U}^1\left(s\right) \\ &\quad + \mathbf{Y^{C+2}}\left(s\right)\left[\mathbf{I} - \mathbf{Z_{s3}}\left(s^-\right)\mathbf{Y_{SIO}}\left(s^-\right)\right]^{-1} \\ &\quad \times \mathbf{Z_{s3}}\left(s^-\right)\mathbf{Y^{C-2}}\left(s^-\right)\mathbf{U}^1\left(s\right) \\ &\quad + \mathbf{Y^{C-2}}\left(s\right)\left[\mathbf{I} - \mathbf{Z_{s3}}\left(s^+\right)\mathbf{Y_{SIO}}\left(s^+\right)\right]^{-1} \\ &\quad \times \mathbf{Z_{s3}}\left(s^+\right)\mathbf{Y^{C+2}}\left(s^+\right)\mathbf{U}^1\left(s\right) \\ &= \left[\mathbf{Y_{SIO}}\left(s\right) + \mathbf{G_c^{-2}}\left(s\right) + \mathbf{G_c^{+2}}\left(s\right)\right]\mathbf{U}^1\left(s\right) \\ &= \mathbf{Y_T}\left(s\right)\mathbf{U}^1\left(s\right) \end{aligned} \quad (24)$$

The matrix $\mathbf{Y_T}$ in (24) is the impedance matrix model of the inverter sub-system obtained by considering the three SIs as a whole during asymmetric fault, which is the foundation for the later parameter and stability analyses. It should be noted that although this impedance model is derived for the scenario with the grounded short-circuit fault occurring in both phase-a and phase-b, it is equally applicable to other fault scenarios as well as to the no-fault scenario. To obtain the impedance matrix of the inverter sub-system in other scenarios, it is sufficient to replace the grid impedance matrix of the corresponding scenario. In particular, the no-fault scenario is a special case of the scenario studied by this paper, as the result of $R_{fault} = \infty$.

In (26), $\mathbf{G_c^{-2}}(s)$ is introduced due to the coupled current at $\omega - 2j\omega_1$ and $\mathbf{G_c^{-2}}(s)$ is introduced due to the coupled current at $\omega + 2j\omega_1$, which can be set to zero if the FCE is ignored. The model developed in the paper can be easily extended to other scenarios with great generality, which can greatly reduce the workload of analyzing system stability in different scenarios.

B. MODEL VERIFICATION

The frequency scanning measurement by perturbation voltages injection is implemented to verify the accuracy of the established impedance model in the frequency domain. By the frequency scanning measurement, the actual impedance results of measurement by the control-hardware-in-loop (CHIL) platform can be achieved as shown in Figure 6, which can be used to compare with the analytical impedance results.

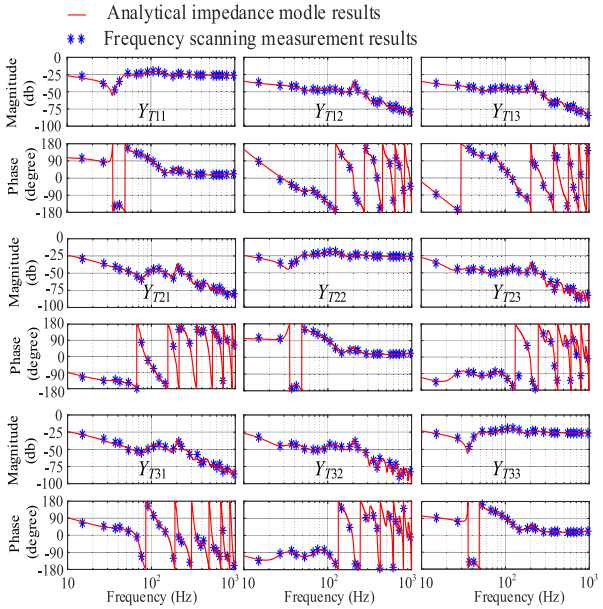

FIGURE 6. Verification of the proposed impedance model of the inverter sub-system.

C. PARAMETERS ANALYSES OF PPCE

The non-zero amplitude of off-diagonal elements in (24) reflects the existence of PPCE between SIs of different phases. The strength of PPCE can be defined as the ratio of the quadratic sum of off-diagonal elements amplitude and the quadratic sum of diagonal elements amplitude [35], which can be expressed as,

$$\varepsilon = \frac{|Y_{T12}|^2 + |Y_{T13}|^2 + |Y_{T21}|^2 + |Y_{T23}|^2 + |Y_{T31}|^2 + |Y_{T32}|^2}{|Y_{T11}|^2 + |Y_{T22}|^2 + |Y_{T33}|^2} \quad (25)$$

Figure 7 shows the curves of ε under different PLL bandwidth f_{PLL}. In Figure 7, there are two crests and one trough in the curves. The frequencies corresponding to the two crests all increase with the increase of f_{PLL}. The frequency corresponding to the trough decrease with increasing the phase-locked loop bandwidth. In addition, the frequency coupling degree near 50 Hz is not affected by f_{PLL}. The frequency coupling degree above 100 Hz is positively correlated with f_{PLL}.

Figure 8 shows the curves of ε when different neutral inductances of the grid $L_{gnt} = L_{dn} + L_{gn}$ used (2mH/ 3mH/ 5mH). From Figure 8, the larger neutral inductance L_{gnt} causes the lager ε. Tus the closeness degree of the coupling

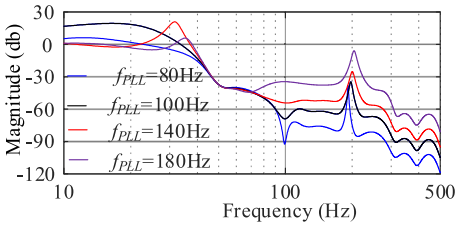

FIGURE 7. The strength of PPCE ε under different PLL bandwidths.

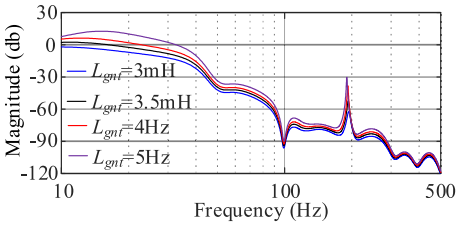

FIGURE 8. The strength of PPCE ε under different neutral inductances L_{gnt}.

relationship between the three phases is positively correlated with the value of the neutral inductance L_{gnt}. This is in line with common sense. In the extreme case, if the neutral line inductance L_{gnt} is zero, there is no coupling relationship between the three phases as shown in Figure 3(a). This also means that the weaker the strength of the grid, the more attention should be paid to the PPCE when performing stability analysis.

IV. STABILITY ANALYSIS OF THREE-PHASE FOUR-WIRE SYSTEM DURING ASYMMETRIC FAULTS

Combining (13) and (24), the system model of the currents of three phases and voltages of three phases at the perturbation frequency can be achieved as (26).

$$\begin{bmatrix} i_{ga}^{1}(s) \\ i_{gb}^{1}(s) \\ i_{gc}^{1}(s) \end{bmatrix} = \left(\mathbf{I} - \mathbf{Y_T}(s)\,\mathbf{Z_{s3}}(s)\right)^{-1}\mathbf{Y_T}(s) \begin{bmatrix} v_{a}^{1}(s) \\ v_{b}^{1}(s) \\ v_{c}^{1}(s) \end{bmatrix}. \quad (26)$$

The system analysis of stability is able to be simplified by means of transforming the system variables in phase domain to the variables in sequence domain. The variable in phase domain can be decomposed into a NS, PS and ZS system component.

$$Defining, \mathbf{S} = \frac{1}{3}\begin{bmatrix} 1 & 1 & 1 \\ 1 & \alpha & \alpha^2 \\ 1 & \alpha^2 & \alpha \end{bmatrix}, \mathbf{S}^{-1} = \begin{bmatrix} 1 & 1 & 1 \\ 1 & \alpha^2 & \alpha \\ 1 & \alpha & \alpha^2 \end{bmatrix} \quad (27)$$

where, $\alpha = e^{j\frac{2\pi}{3}} = -\frac{1}{2} + j\frac{\sqrt{3}}{2}$.

By matrix operations, (28) can be transferred as,

$$\begin{bmatrix} i_0(s) \\ i_1(s) \\ i_2(s) \end{bmatrix} = \left(\mathbf{I} - \mathbf{Y_{T012}}(s)\,\mathbf{Z_{s012}}(\mathbf{s})\right)^{-1}\mathbf{Y_{T012}}(s) \begin{bmatrix} v_0(s) \\ v_1(s) \\ v_2(s) \end{bmatrix} \quad (28)$$

$$\mathbf{Y_{T012}}(s) = \mathbf{S}\mathbf{Y_T}(s)\,\mathbf{S}^{-1} \quad (29)$$

$$\mathbf{Z_{S012}}(s) = \mathbf{S}\mathbf{Z_{S3}}(s)\,\mathbf{S}^{-1}. \quad (30)$$

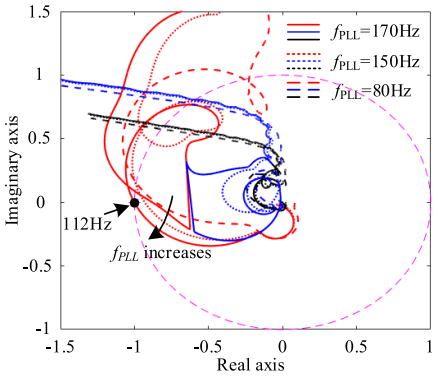

FIGURE 9. Nyquist curves of $\zeta 1$, $\zeta 2$ and $\zeta 3$ when $f_{PLL} = 80$Hz, $f_{PLL} = 150$Hz and $f_{PLL} = 170$Hz.

It should be noted that the matrices in equation (30) are diagonal matrices when the system is completely symmetric. And the stability of the system can be analyzed independently by PS, NS and ZS SISO models. However, when the system is not symmetric, there will be a coupling relationship between the ZS PS and NS impedances, and then the stability of the system will be analyzed by the Generalized Nyquist Criterion (GNC) [36].

The stability of the system is determined by whether the Nyquist curves of the three eigenvalues $\zeta 1$, $\zeta 2$, and $\zeta 3$ of the impedance ratio matrix $\mathbf{Y_{T012}Z_{S012}}$ encircle the point $(-1, j0)$ according to the GNC theory. These eigenvalues can be calculated by solving the equation $det(\lambda \mathbf{E}–\mathbf{Y_{T012}Z_{S012}}) = 0$.

In the paper, the fault resistance value R_{Fault} is adopted to weigh the fault degree, the larger the fault resistance value means the weaker the fault degree. When $R_{Fault} = \infty$, it means that there is no short circuit fault.

A. EFFECT OF PLL BANDWIDTH ON SYSTEM STABILITY

Figure 9 shows the Nyquist curves of $\zeta 1$, $\zeta 2$ and $\zeta 3$ when $f_{PLL} = 80$Hz, $f_{PLL} = 150$Hz, $f_{PLL} = 170$Hz, and $R_{Fault} = 0.8\Omega$. It can be seen from Figure 9 that as f_{PLL} gradually increases, Nyquist curves $\zeta 1$ gradually approach $(-1,0)$. When $f_{PLL} = 170$Hz, the Nyquist curve $\zeta 1$ surrounds $(-1,0)$ and intersects with the unit circle at 112 Hz. It indicates that the system will destabilize at 112 Hz. This indicates that reduced PLL bandwidth contributes to improving the system stability under asymmetry faults.

B. EFFECT OF ASYMMETRIC SHORT CIRCUIT FAULT DEGREE ON SYSTEM STABILITY

Figure 10 shows the Nyquist curves of $\zeta 1$, $\zeta 2$, and $\zeta 3$ with $f_{PLL} = 80$Hz and $\sigma = 1$ when $R_{Fault} = 2\Omega$, $R_{Fault} = 0.8\Omega$, and $R_{Fault} = 0.4\Omega$. From Figure 10, as R_{Fault} gradually decreases, asymmetric fault degree, Nyquist curves $\zeta 1$ gradually approach $(-1,0)$. When $R_{Fault} = 0.4\Omega$, the Nyquist curve $\zeta 1$ surrounds $(-1, 0)$ and intersects with the unit circle at 82 Hz. This indicates that the system will become unstable at 82 Hz. The law indicates that the deeper the fault, the more likely it is to cause system instability under the same controller parameters during asymmetry faults.

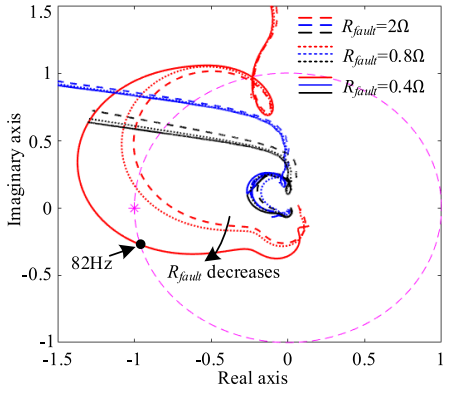

FIGURE 10. The Nyquist curves of $\zeta 1$, $\zeta 2$ and $\zeta 3$ when $R_{Fault} = 2\Omega$, $R_{Fault} = 0.8\Omega$, and $R_{Fault} = 0.4\Omega$ respectively.

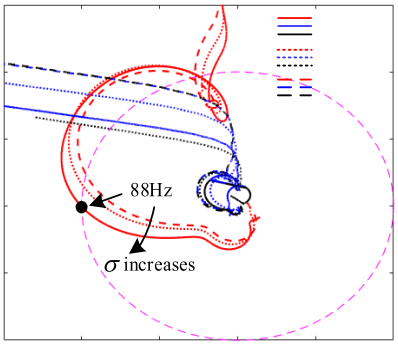

FIGURE 11. The Nyquist curves of $\zeta 1$, $\zeta 2$ and $\zeta 3$ when $\sigma = 0.03$, $\sigma = 1$ and $\sigma = 39$.

C. EFFECT OF SHORT CIRCUIT LOCATION ON SYSTEM STABILITY ASYMMETRIC SHORT CIRCUIT FAULT DEGREE

Defining $\sigma = L_{gx}/L_{dx}$, σ denotes the short circuit location. a smaller coefficient σ means that the location of short circuit fault is further away from inverters. Figure 11 shows the Nyquist curves of $\zeta 1$, $\zeta 2$ and $\zeta 3$ with $f_{PLL} = 80$Hz and $R_{Fault} = 0.8\Omega$ when $\sigma = 0.03, \sigma = 1$, and $\sigma = 39$. From Figure11, as σ gradually increases, the stability margin of the system gradually decreases. And when σ increases to 39, the curve $\zeta 1$ intersects with the point $(-1,0)$ at 88 Hz. This indicates that the system will become unstable at 88 Hz. This also shows that the closer the short circuit fault is to the inverter, the more likely it is to result in small signal instability during asymmetry faults.

V. EXPERIMENTAL RESULTS

To better validate the above theoretical analysis, the experimental platform is established as expressed in Figure 12. The hardware platform consists of two parts, the control part based on TMS320F28335+FPGA control board and the main circuit part based on Typhoon 602+. The control part is to realize the role of performing sampling, calculation, control and PWM generation, and Typhoon 602+ is used to simulate the main circuit of the SIs as well as the grid. The experimental parameters can be seen in Table 1.

Figure 13 shows the verification waveform about the effect of the PLL bandwidth on the system stability. Figure 13 is divided into three states. State ① shows active power, reactive

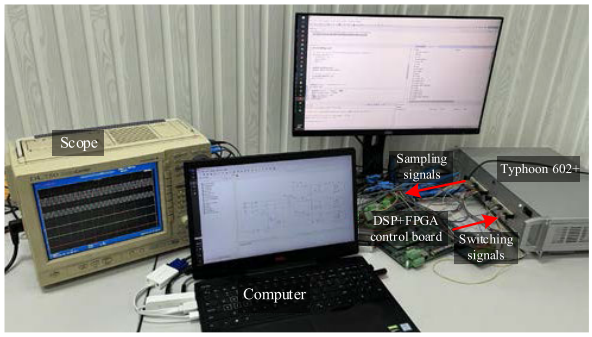

(a)

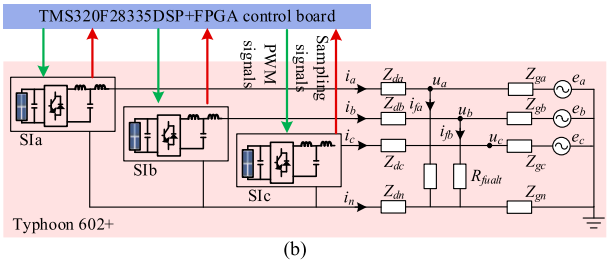

(b)

FIGURE 12. Experimental platform.

TABLE 1. Parameters of single-phase inverters-based power system.

DEFINITION	Value	DEFINITION	Value
Rated dc voltage V_{dc}	800 V	Switching frequency f_s	15 kHz
Rated frequency f_1	50 Hz	Bandwidth of PLL f_{PLL}	80 Hz
Rated ac voltage V_{abc}	380 V	Resonant gain of PR current controller k_{cr}	600
Inductance/parasitic L_1//R_1	0.75mH/0.1Ω	Proportional gain of PR current controller k_{cp}	9
Inductance/parasitic L_2//R_2	0.45mH/0.1Ω	PCC voltage feed forward control coefficient G_f	0.6
Capacitor/parasitic C/R_3	6.8 μF/0.1Ω	Active damping coefficient k_c	6
Grid impedance 1 $L_{da,b,c,n}$/$R_{da,\,b,\,c,\,n}$	2 mH/0.05 Ω	Amplitude of current reference I_{ref}	45 A
Grid impedance 2 $L_{ga,\,b,\,c,\,n}$/$R_{ga,\,b,\,c,\,n}$	2 mH/0.05 Ω	Fault branch impedance R_{fault}	0.8 Ω

power, voltages, and currents of the PCC during normal operation. It can be seen from the figure that all three phases of inverters operate stably. State ② shows the experimental waveform when the grounded short-circuit fault occurs in both phase-a and phase-b with $f_{PLL} = 80$Hz, $R_{fault} = 0.8\Omega$, and $\sigma = 1$. It can be seen from the figure that after a dynamic process of about 100ms, the three single-phase inverters resume steady-state operation, the ZS component of 50Hz in the system increases significantly, and there is no obvious harmonic component in the system. State ③ shows the experimental waveform when the f_{PLL} changes from 80Hz to 170Hz with $R_{fault} = 0.8\ \Omega$ and $\sigma = 1$.

From Figure 13 the system gradually diverges as f_{PLL} increases, and there are obvious harmonic components in the system at 12Hz, 112Hz and 212Hz. The frequencies of the harmonic components are consistent with the harmonic frequencies predicted in Figure 9. Therefore, comparing state ② and state ③, it can be observed that the larger PLL bandwidth is, the more likely it is to result in system instability when the short-circuit location $\sigma = 1$ and the degree of short-circuit fault $R_{fault} = 0.8\Omega$ are guaranteed to be the same. The

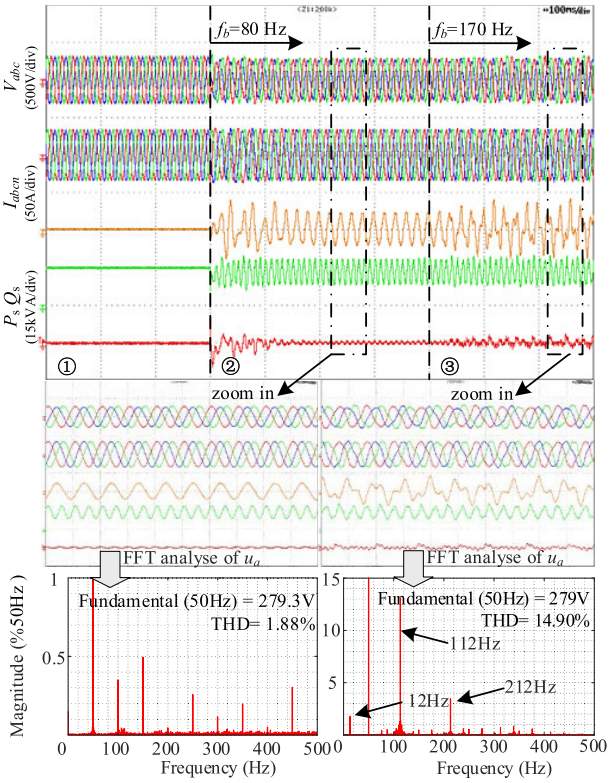

FIGURE 13. Verification waveform of the effect of the PLL bandwidth on the system stability.

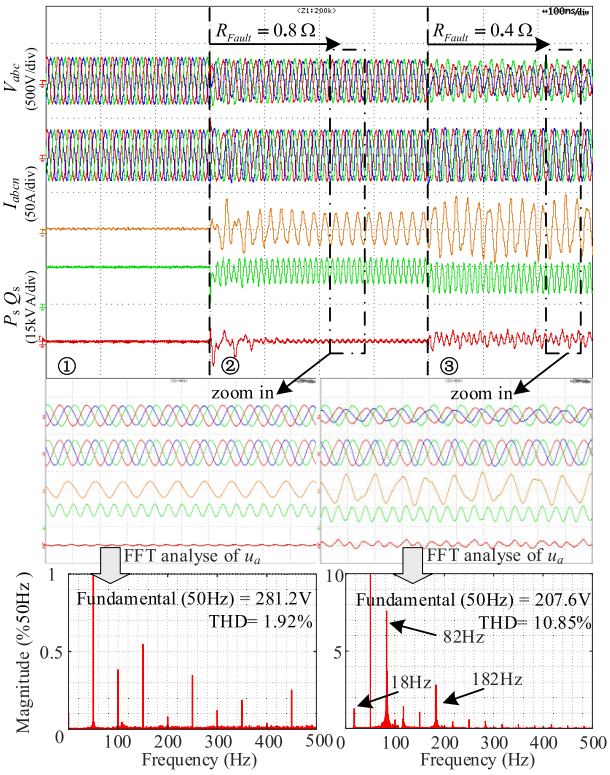

FIGURE 14. Verification waveform about the effect of the short fault degree on the system stability.

experimental results coincide to the theoretical results expressed in Figure 9.

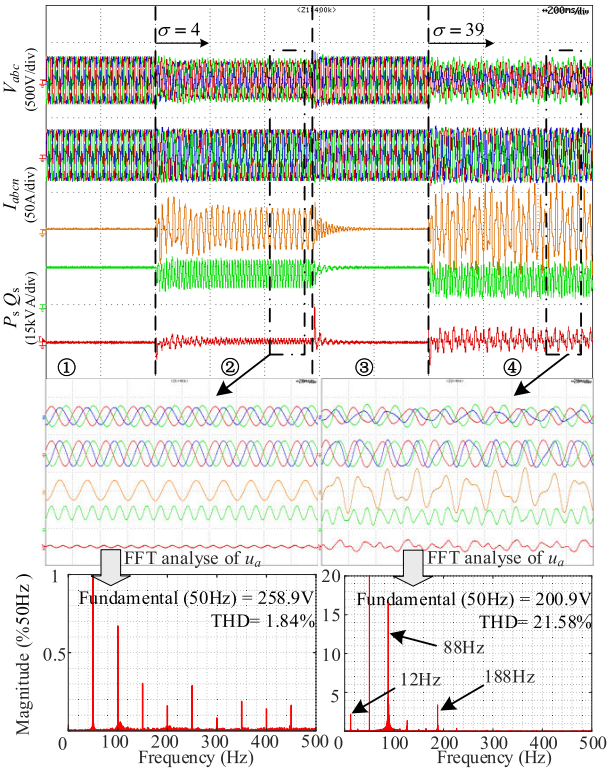

FIGURE 15. Verification waveform of the effect of short circuit location on system stability.

Figure 14 gives the validated waveforms about the effect of the fault degree of the short circuit fault on the system stability. Figure 14 is also divided into three states. State ① shows the waveforms of the system during the stable operation state. It can be seen from the figure that all three phases inverters operate stably and there is no obvious harmonic component in the system. State ② shows the experimental waveform when the grounded short-circuit fault occurs in both phase-a and phase-b with $f_{PLL} = 80$Hz, $R_{fault} = 0.8\Omega$ and $\sigma = 1$. It can be seen from the figure that after a dynamic process about 100ms, the three single-phase inverters resume steady-state operation, the ZS component of 50Hz in the system increases significantly, and there is no obvious harmonic component in the system. State ③ shows the experimental waveform when R_{fault} changes from 0.8Ω to 0.4Ω with $f_{PLL} = 80$Hz and $\sigma = 1$.

From Figure 14, there are obvious harmonic components in the system, and the harmonic component frequencies are 18Hz, 82Hz, and 182Hz as shown by the FFT analysis. The harmonic components' frequencies are consistent with the frequencies predicted in Figure 10. Therefore, comparing state ② and state ③, it can be observed that the greater the short circuit fault degree is, the more likely it is to result in system instability when PLL bandwidth and short-circuit location are guaranteed to be the same. And these experimental results coincide with theoretical analysis results expressed in Figure 10.

The effect of short circuit location on system stability is shown in Figure 15. The figure is divided into four states.

State ① indicates the waveforms of the system during the stable operation state. It can be seen from the figure that all three phases inverters operate stably. State ② shows experimental waveform when the grounded short-circuit fault occurs in both phase-a and phase-b with $f_{PLL} = 80\text{Hz}$, $R_{fault} = 0.8\Omega$ and $\sigma = 4$ From the figure, it can be seen that after a dynamic process of about 200ms, the three-phase inverters resume steady-state operation, and the ZS component of 50Hz in the system increases significantly, and there is no obvious harmonic component in the system. State ③ shows the experimental waveform when a short-circuit to ground fault has been cleared. From State ③, the system stabilizes after about 200ms. State ④ shows experimental waveform when the grounded short-circuit fault occurs in both phase-a and phase-b with $f_{PLL} = 80\text{Hz}$, $R_{fault} = 0.8\Omega$ and $\sigma = 39$.

From State ④, there are obvious harmonic components in the system, and the harmonic component frequency in the system are 12Hz, 88Hz and 188Hz as shown by the FFT analysis. The frequencies of harmonic components are consistent with the frequencies predicted as Figure 11. Therefore, comparing state ② and state ④, it can be found that the closer grid fault location to the inverter, the more likely it is to result in system instability when the control parameters are guaranteed to be the same. The experimental results coincide to the theoretical analysis results expressed in Figure 11.

These experiments demonstrate that the impedance model considering the PPCE and FCE proposed in this paper can be used to evaluate the system stability accurately.

VI. CONCLUSION

Theoretical research and experiments have been carried out in this paper to study the stability of SIs connected to the three-phase four-wire weak grid under asymmetric faults. The conclusions can be seen as follows,

(1) In the system where the SIs are divided into three phase groups and connected to the three-phase four-wire weak grid under asymmetrical fault conditions, the PPCE, FCE, and asymmetric grid impedance can be analyzed by considering the SIs as an inverter sub-system. And the admittance model considering PPCE, FCE, and asymmetric grid has been established by harmonic transfer matrix.

(2) Based on the established admittance model, the main factors that affect the PPCE are the PLL bandwidth and the neutral inductance L_{gnt}. The larger PLL bandwidth or the larger neutral inductance L_{gnt} brings stronger PPCE. This also means that the weaker strength of the grid, the more attention should be paid to the PPCE when performing stability analysis.

(3) Based on the achieved impedance model, the small-signal stability analysis of the system during asymmetric fault has been analyzed accurately. The study results indicate that the reduced PLL bandwidth contributes to improving the small-signals stability. And the deeper the short circuit fault degree, the more likely it is to cause system instability at the same controller parameters. In addition, a closer location of the fault to the inverter will deteriorate the system stability under asymmetric faults.

Overall, the paper focus on the factors and laws that impacts the system's small-signal stability, without proposing strategies for enhancing it. Therefore, the next step for the authors would be to explore how to improve system stability through the rational design of inverters parameters or the proposal of new control strategies.

REFERENCES

[1] A. R. Malekpour, A. Pahwa, and B. Natarajan, "Hierarchical architecture for integration of rooftop PV in smart distribution systems," *IEEE Trans. Smart Grid*, vol. 9, no. 3, pp. 2019–2029, May 2018.

[2] S. A. E. Batawy and W. G. Morsi, "Optimal secondary distribution system design considering rooftop solar photovoltaics," *IEEE Trans. Sustain. Energy*, vol. 7, no. 4, pp. 1662–1671, Oct. 2016.

[3] A. M. M. Nour, A. Y. Hatata, A. A. Helal, and M. M. El-Saadawi, "Review on voltage-violation mitigation techniques of distribution networks with distributed rooftop PV systems," *IET Gener., Transmiss. Distrib.*, vol. 14, no. 3, pp. 349–361, Feb. 2020.

[4] M. Zeraati, M. E. H. Golshan, and J. M. Guerrero, "Voltage quality improvement in low voltage distribution networks using reactive power capability of single-phase PV inverters," *IEEE Trans. Smart Grid*, vol. 10, no. 5, pp. 5057–5065, Sep. 2019.

[5] Q. Chai, C. Zhang, Y. Xu, and Z. Y. Dong, "PV inverter reliability-constrained volt/var control of distribution networks," *IEEE Trans. Sustain. Energy*, vol. 12, no. 3, pp. 1788–1800, Jul. 2021.

[6] A. Mokaribolhassan, G. Nourbakhsh, G. Ledwich, A. Arefi, and M. Shafiei, "Distribution system state estimation using PV separation strategy in LV feeders with high levels of unmonitored PV generation," *IEEE Syst. J.*, vol. 17, no. 1, pp. 684–695, Mar. 2023, doi: 10.1109/JSYST.2022.3155164.

[7] A. Zahedmanesh, K. M. Muttaqi, and D. Sutanto, "An adaptable correlated control for maintaining voltage quality in low-voltage distribution grids containing PVs and PEVs," *IEEE Trans. Ind. Informat.*, vol. 18, no. 9, pp. 5804–5814, Sep. 2022.

[8] R. Torquato, D. Salles, C. O. Pereira, P. C. M. Meira, and W. Freitas, "A comprehensive assessment of PV hosting capacity on low-voltage distribution systems," *IEEE Trans. Power Del.*, vol. 33, no. 2, pp. 1002–1012, Apr. 2018.

[9] Y. Ren, X. Wang, L. Chen, Y. Min, G. Li, L. Wang, and Y. Zhang, "A strictly sufficient stability criterion for grid-connected converters based on impedance models and Gershgorin's theorem," *IEEE Trans. Power Del.*, vol. 35, no. 3, pp. 1606–1609, Jun. 2020.

[10] K. Liao, B. Pang, J. Yang, and Z. He, "Compensation strategy of wide-band voltage harmonics for doubly-fed induction generator," *IEEE Trans. Energy Convers.*, vol. 38, no. 1, pp. 674–684, Mar. 2023.

[11] S. Behzadirafi and F. de León, "Closed-form determination of the impedance locus plot of fault current limiters: A rigorous approach with graphical representation," *IEEE Trans. Power Del.*, vol. 33, no. 6, pp. 2710–2717, Dec. 2018.

[12] R. S. R. Sankar, S. V. J. Kumar, and G. M. Rao, "Impedance based stability analysis of single-phase PV inverter connected to weak grid with voltage feed forward control," in *Proc. IEEE Int. Conf. Power, Control, Signals Instrum. Eng. (ICPCSI)*, Sep. 2017, pp. 2187–2194.

[13] C. Zhang, X. Wang, and F. Blaabjerg, "Analysis of phase-locked loop influence on the stability of single-phase grid-connected inverter," in *Proc. IEEE 6th Int. Symp. Power Electron. Distrib. Gener. Syst. (PEDG)*, Jun. 2015, pp. 1–8.

[14] Y. Liao, Z. Liu, H. Zhang, and B. Wen, "Low-frequency stability analysis of single-phase system with dq-frame impedance approach—Part I: Impedance modeling and verification," *IEEE Trans. Ind. Appl.*, vol. 54, no. 5, pp. 4999–5011, Sep. 2018.

[15] Y. Liao, Z. Liu, H. Zhang, and B. Wen, "Low-frequency stability analysis of single-phase system with dq-frame impedance approach—Part II: Stability and frequency analysis," *IEEE Trans. Ind. Appl.*, vol. 54, no. 5, pp. 5012–5024, Oct. 2018.

[16] S. Lissandron, L. D. Santa, P. Mattavelli, and B. Wen, "Experimental validation for impedance-based small-signal stability analysis of single-phase interconnected power systems with grid-feeding inverters," *IEEE J. Emerg. Sel. Topics Power Electron.*, vol. 4, no. 1, pp. 103–115, Mar. 2016.

[17] A. Sangwongwanich, Y. Yang, D. Sera, H. Soltani, and F. Blaabjerg, "Analysis and modeling of interharmonics from grid-connected photovoltaic systems," *IEEE Trans. Power Electron.*, vol. 33, no. 10, pp. 8353–8364, Oct. 2018.
[18] Q. Qian, S. Xie, J. Xu, K. Xu, S. Bian, and N. Zhong, "Output impedance modeling of single-phase grid-tied inverters with capturing the frequency-coupling effect of PLL," *IEEE Trans. Power Electron.*, vol. 35, no. 5, pp. 5479–5495, May 2020.
[19] C. Zhang, M. Molinas, S. Føyen, J. A. Suul, and T. Isobe, "Harmonic-domain SISO equivalent impedance modeling and stability analysis of a single-phase grid-connected VSC," *IEEE Trans. Power Electron.*, vol. 35, no. 9, pp. 9770–9783, Sep. 2020.
[20] J. Lin, M. Su, Y. Sun, D. Yang, and S. Xie, "Recursive SISO impedance modeling of single-phase voltage source rectifiers," *IEEE Trans. Power Electron.*, vol. 37, no. 2, pp. 1296–1309, Feb. 2022.
[21] X. Liu, X. Chen, M. Shahidehpour, C. Li, Q. Wu, Y. Wu, and J. Wen, "Active fault current limitation for low-voltage ride-through of networked microgrids," *IEEE Trans. Power Del.*, vol. 37, no. 2, pp. 980–992, Apr. 2022.
[22] G. Pannell, D. J. Atkinson, and B. Zahawi, "Minimum-threshold crowbar for a fault-ride-through grid-code-compliant DFIG wind turbine," *IEEE Trans. Energy Convers.*, vol. 25, no. 3, pp. 750–759, Sep. 2010.
[23] X. Wang, J. Yao, J. Pei, P. Sun, H. Zhang, and R. Liu, "Analysis and damping control of small-signal oscillations for VSC connected to weak AC grid during LVRT," *IEEE Trans. Energy Convers.*, vol. 34, no. 3, pp. 1667–1676, Sep. 2019.
[24] J. Hu, B. Wang, W. Wang, H. Tang, Y. Chi, and Q. Hu, "Small signal dynamics of DFIG-based wind turbines during riding through symmetrical faults in weak AC grid," *IEEE Trans. Energy Convers.*, vol. 32, no. 2, pp. 720–730, Jun. 2017.
[25] Ö. Göksu, R. Teodorescu, C. L. Bak, F. Iov, and P. C. Kjaer, "Instability of wind turbine converters during current injection to low voltage grid faults and PLL frequency based stability solution," *IEEE Trans. Power Syst.*, vol. 29, no. 4, pp. 1683–1691, Jul. 2014.
[26] S. Mortazavian, M. M. Shabestary, and Y. A. I. Mohamed, "Analysis and dynamic performance improvement of grid-connected voltage-source converters under unbalanced network conditions," *IEEE Trans. Power Electron.*, vol. 32, no. 10, pp. 8134–8149, Oct. 2017.
[27] Z. Yang, W. Liao, Q. Zhang, C. L. Bak, and Z. Chen, "Fault coordination control for converter-interfaced sources compatible with distance protection during asymmetrical faults," *IEEE Trans. Ind. Electron.*, vol. 70, no. 7, pp. 6941–6952, Jul. 2023.
[28] C. Zhang, M. Molinas, A. Rygg, J. Lyu, and X. Cai, "Harmonic transfer-function-based impedance modeling of a three-phase VSC for asymmetric AC grid stability analysis," *IEEE Trans. Power Electron.*, vol. 34, no. 12, pp. 12552–12566, Dec. 2019.
[29] Y. Liao, X. Wang, X. Yue, and L. Harnefors, "Complex-valued multi-frequency admittance model of three-phase VSCs in unbalanced grids," *IEEE J. Emerg. Sel. Topics Power Electron.*, vol. 8, no. 2, pp. 1934–1946, Jun. 2020.
[30] R. Liu, J. Yao, P. Sun, J. Pei, H. Zhang, and Y. Zhao, "Complex impedance-based frequency coupling characteristics analysis of DFIG-based WT during asymmetric grid faults," *IEEE Trans. Ind. Electron.*, vol. 68, no. 9, pp. 8274–8288, Sep. 2021.
[31] Z.-X. Zhu and M.-S. Chiu, "Dynamic analysis of decentralized 2 × 2 control systems in relation to loop interaction and local stability," *Ind. Eng. Chem. Res.*, vol. 37, no. 2, pp. 464–473, Feb. 1998.
[32] B. Hu, H. Nian, M. Li, Y. Liao, J. Yang, and H. Tong, "Synchronization stability enhancement of grid-following converter under inductive power grid," *IEEE Trans. Energy Convers.*, vol. 38, no. 2, pp. 1485–1488, Jun. 2023.
[33] X. Wang, F. Blaabjerg, and P. C. Loh, "Virtual RC damping of LCL-filtered voltage source converters with extended selective harmonic compensation," *IEEE Trans. Power Electron.*, vol. 30, no. 9, pp. 4726–4737, Sep. 2015.
[34] Q. Qian, S. Xie, L. Huang, J. Xu, Z. Zhang, and B. Zhang, "Harmonic suppression and stability enhancement for parallel multiple grid-connected inverters based on passive inverter output impedance," *IEEE Trans. Ind. Electron.*, vol. 64, no. 9, pp. 7587–7598, Sep. 2017.
[35] H. Nian, Y. Liu, H. Li, B. Hu, Y. Liao, and J. Yang, "Commutation overlap characteristic modeling and stability analysis of LCC-HVDC in sending AC grid," *IEEE Trans. Sustain. Energy*, vol. 13, no. 3, pp. 1594–1606, Jul. 2022.
[36] Y. Xu, H. Nian, T. Wang, L. Chen, and T. Zheng, "Frequency coupling characteristic modeling and stability analysis of doubly fed induction generator," *IEEE Trans. Energy Convers.*, vol. 33, no. 3, pp. 1475–1486, Sep. 2018.

YUMING LIAO was born in Ganzhou, Jiangxi, China. He received the M.Eng. degree in electronics and power transmission from the Department of Electrical Engineering, Hefei University of Technology, Hefei, China, in 2018. He is currently pursuing the Ph.D. degree in electrical engineering with Zhejiang University, Hangzhou, China.

His research interests include stability analysis of grid-connected operations and wind power generation systems.

HENG NIAN (Senior Member, IEEE) received the B.Eng. and M.Eng. degrees in electrical engineering from the Hefei University of Technology, China, in 1999 and 2002, respectively, and the Ph.D. degree in electrical engineering from Zhejiang University, China, in 2005.

From 2005 to 2007, he was a Postdoctoral Researcher with the College of Electrical Engineering, Zhejiang University. In 2007, he was promoted as an Associate Professor. From 2013 to 2014, he was a Visiting Scholar with the Department of Electrical, Computer, and System Engineering, Rensselaer Polytechnic Institute, Troy, NY, USA. Since 2016, he has been a Full Professor with the College of Electrical Engineering, Zhejiang University. He has published more than 40 IEEE/IET transaction papers and holds more than 20 issued/pending patents. His current research interests include optimal design and operation control for wind power generation systems.

YAOXIN WANG (Student Member, IEEE) was born in Changzhi, China. He received the B.Eng. degree in electrical engineering from Zhejiang University, Hangzhou, China, in 2021, where he is currently pursuing the M.Eng. degree in electrical engineering.

His research interests include dc-impedance-based stability analysis methods for VSCs-based power systems under weak grids and the corresponding impedance reshaping control strategy.

DAN SUN (Senior Member, IEEE) received the B.S. degree in electrical engineering from Shenyang Jianzhu University, Shenyang, China, in 1997, the M.S. degree in electrical engineering from Hohai University, Nanjing, China, in 2000, and the Ph.D. degree in electrical engineering from Zhejiang University, Hangzhou, China, in 2004.

In 2004, she joined the College of Electrical Engineering, Zhejiang University. Since 2017, she has been a Full Professor with Zhejiang University. Her research interests include advanced electric machine drives and control for wind power generation systems.